



Science Arts & Métiers (SAM)

is an open access repository that collects the work of Arts et Métiers Institute of Technology researchers and makes it freely available over the web where possible.

This is an author-deposited version published in: <https://sam.ensam.eu>
Handle ID: <http://hdl.handle.net/10985/20263>

To cite this version :

Laurent PELTIER, Sophie BERVEILLER, Fodil MERAGHNI, Paul LOHMULLER, Pascal LAHEURTE - Martensite Transformation and Superelasticity at High Temperature of (TiHfZr)₇₄(NbTa)₂₆ High-Entropy Shape Memory Alloy - Shape Memory and Superelasticity p.in press - 2021

Any correspondence concerning this service should be sent to the repository

Administrator : scienceouverte@ensam.eu



Martensite Transformation and Superelasticity at High Temperature of (TiHfZr)₇₄(NbTa)₂₆ High-Entropy Shape Memory Alloy

L. Peltier¹ · S. Berveiller¹ · F. Meraghni¹  · P. Lohmuller² · P. Laheurte²

Abstract In this work, a (TiHfZr)(NbTa)₂₆ (%at) high-entropy quinary alloy has been developed especially for high-temperature superelastic applications and studied over a large range of temperatures. The mechanical properties of this new material were compared with those of other superelastic alloys. The different ingots have been made in a cold crucible from pure metals. Several thermomechanical treatments have been performed on the microstructure of four alloys among them (TiHfZr)(NbTa)₂₆ alloy. The microstructure of each alloy has been characterized by differential scanning calorimetry (DSC), scanning electron microscopy (SEM), and x-ray diffraction technique (XRD) and the mechanical behavior was investigated through three-point bending tests between -40 and 200 °C, in quasi-static monotonic and low cycle loading conditions. The effects of the thermomechanical treatments on the static and cyclic thermomechanical mechanical responses have been analyzed in combination with the microstructure investigations of the four studied alloys. It has been shown that the (TiHfZr)(NbTa)₂₆ alloy presents a martensitic transformation and a superelastic effect over the studied range of temperatures, in the cold-worked state or after solution treatment. Finally, the obtained experimental results have been compared with those of other superelastic

alloys demonstrating the features of the developed high-entropy high-temperature superelastic alloy.

Keywords High-entropy alloy · High-temperature shape memory alloy · Superelasticity and pseudoelasticity behavior · Thermal three-point bending test · Martensitic transformation

Introduction

Ternary or quaternary shape memory alloys (SMAs) based on TiNb compositions have been extensively studied [1–5]. To combine with the high-entropy effect, a fifth element has to be added. In 2015, Firstov et al. have evidenced a reversible martensitic transformation and shape memory effect in TiHfZrNiCu [6, 7] and TiHfZrCoNiCu [8] high-entropy alloys (HEAs). Yaacoub et al. [9] have studied the superelastic behavior of a (TiZrHf)₅₀Ni₂₅Co₁₀Cu₁₅ alloy over a wide range of deformation temperatures, standing from -75 °C up to 100 °C, during the compression test. The alloy exhibited stress transformation up to 1200 MPa at a higher temperature. These previous alloys are known as “NiTi-like alloys” [10]. Wang et al. [11] have developed a TiNbAl-like alloy that exhibits superelastic behavior at room temperature with a recoverable strain around 5%, by optimizing thermal treatments and Nb content of the TiZrHfAlNb high-entropy alloy. Other superelastic HEAs have been developed, e.g., a FeNiCoAlTaB alloy [12], that combine also high damping and cryogenic properties. High-temperature HE-SMA effect was obtained on a (NiPd)₅₀(TiHfZr)₅₀ alloy [13], as well as on a NiCuTiHf_{0.6}Zr_{0.4} alloy [14].

So far, up to our knowledge, no Ti-26Nb-like high-entropy alloy has been developed for superelastic behavior.

✉ F. Meraghni
fodil.meraghni@ensam.eu

¹ LEM3, Arts et Métiers Institute of Technology, Université de Lorraine, UMR 7239 CNRS, HESAM Université, 4, rue Augustin Fresnel, 57070 Metz, France

² LEM3, Université de Lorraine, Arts et Métiers Institute of Technology, UMR 7239 CNRS, 7, rue Félix Savart, 57070 Metz, France

The mechanical properties of an equiatomic TiHfZrNbTa alloy were studied by Dirras et al. at room temperature [15] and by Feuerbacher et al. at high temperature [16]. This alloy corresponds to a Ti-40Nb-like one and it does not exhibit any memory effect, nor superelasticity or pseudoelasticity; it has very high mechanical properties even at high temperatures (up to 300 °C). Moreover, their workability remains very good despite high resistance strength.

The present work aims at developing a HEA-SMA alloy with superelastic behavior over a large range of temperature. To this end, a new non-equiatom composition (TiHfZr)(NbTa)₂₆ has been studied and thermomechanically characterized. This alloy is a Ti-26Nb-like alloy; it will be called so in what follows. It is worth reminding that Ti-26Nb alloys are employed for biomedical applications due to their low Young modulus [17–19]. The mechanical behavior has been characterized by three-point bending tests in static and cyclic conditions, at different temperatures ranging from – 40 °C up to 200 °C. Two other commercial alloys were considered for comparison, namely, Ni₅₁Ti₄₉ alloy from Nimesis Technology company and BETA III alloy from Cezus UGINE company. The first alloy is known for its high superelastic behavior [20] and has been used as a reference alloy for the comparison. The second one presents athermal properties over a temperature ranging from – 20 to 100 °C [21–23].

In the first part of the paper, the chemical composition of the high-entropy and superelastic alloy (HE and SEAs) is presented and motivated based on microstructural criteria. In the second section alloying processing, mechanical and thermal characterization is detailed, notably in terms of phase transformation. In the third section, experimental results are presented and discussed with respect to the microstructure and mechanical properties of different alloys. A comparative discussion summarizes the obtained results in order to position them with respect to the related bibliographic context, with special attention to the temperature dependence of the four investigated alloys. In conclusion, some concluding remarks highlight the experimental findings and hence the interest in developed HEA-SEA.

Motivations of the Composition of the High-Entropy Superelastic Alloy

The main high-temperature shape memory alloys (HT-SMAs) employed could have a ternary composition as NiTi-X, CuAl-X, FeMn-X, and TiNb-X where X stands for a chemical element. In one of the earlier works, Cantor et al. [24] have defined that high-entropy alloys (HEA) must contain at least five chemical elements with an atomic concentration between 5 and 35 at.% [23, 24]. Therefore,

for a HEA-SMA, it is mandatory to substitute a partial fraction of one or more elements of the SMAs initial composition by adding two or more other elements. Equivalent elements are then chosen according to five criteria that have been established by analyzing different HEA-SMA [5, 6, 12, 25–29]. These five criteria are, respectively, given as follows: the covalence radius, the Pauling electronegativity, the melting and evaporation temperatures, and the thermal conductivity of the equivalent element. These characteristics (related to the five criteria) must have values close (or within the acceptable range) to the values of the element that should be substituted or partially replaced. Figure 1 presents the equivalent element for the main five chemical elements constitutive of SMA. In the case of the TiNb binary alloy, Ti can be partially replaced by Hf and Zr, whereas Nb can be partially replaced by Ta. Consequently, the Ti_yNb_{100–y} alloy is then transformed into (TiHfZr)_y(NbTa)_{100–y} alloy [15, 30, 31]. Derived from the works of Zhan et al. [32] and Podolskiy et al. [33], one alloy composition that can be proposed is Ti₃₀Hf₁₉Zr₂₅-(NbTa)₂₆ (in at.%). In what follows, the studied alloy will be thus this composition.

Besides the specific chemical composition, high-entropy alloys should verify five other criteria derived from the work of Hume-Rothery [34], to avoid the formation of metallic glass and ensure the formation of a solid solution [35–38]: first, the mixing entropy (ΔS_{mix}) has to be $> 1.5R$, where R is the gas constant [25]. The second criterion deals with the difference of atomic radius (R_a) of the elements in the alloy composition that must ensure a lattice distortion (δ) $< 6\%$. Thirdly, the mixing enthalpy, ΔH_{mix} , estimated by averaging the mixing enthalpies of all binary alloys composed by each pair of composition elements, should be $< 10 \text{ kJ mol}^{-1}$ in absolute value. It must be noted that a zero or close-to-zero ΔH_{mix} will promote the development of a solid solution during alloy solidification. The fourth criterion is based on the difference of electronegativity between all the constitutive elements, while the last criterion is related to the average of the valence electrons (VEC). These last two criteria are applied to predict the type of lattice resulting from solidification [39].

Table 1 shows the HEA criterion values for different alloys. The Ti₃₀Hf₁₉Zr₂₅-(NbTa)₂₆ alloy investigated in this study has been chosen since it fulfills all the criteria. Thus, one can expect the formation of a solid solution and compare it to CoCrFeMnNi alloys with potentially good cold workability [24]. The BETA III alloy which is also a quinary alloy does not fulfill any of the five criteria as shown in Table 1.

Fig. 1 Periodic table showing the different equivalent elements for those commonly used in SMAs compositions

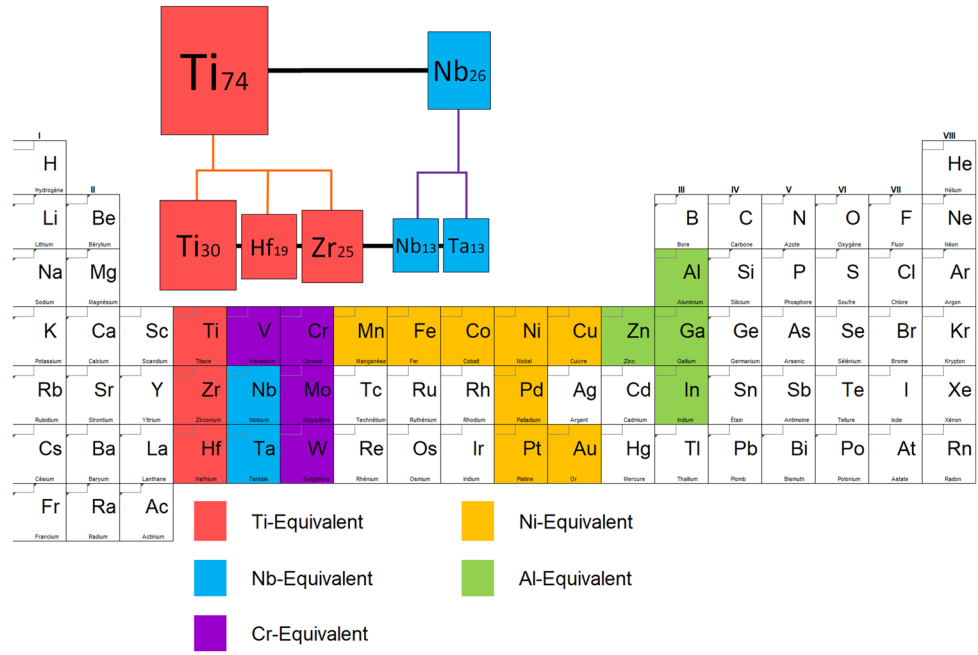


Table 1 Criteria for microstructures formation, ΔS_{mix} and ΔH_{mix} correspond to mixing entropy and enthalpy, respectively, δ corresponds to the relative radii difference, EN means electronegativity, whereas VEC stands for valence electronic concentration

Alloys	ΔS_{mix} $x > 1.5$	ΔH_{mix} (kJ/mol) $x \in [-10; 10]$	δ (%) $x \in [0; 6.6]$	EN Pauling $x \approx 0$	VEC $x \neq [6.87; 7.99]$
CrMnFeCoNi [24]	1.61 <input checked="" type="checkbox"/>	-4.16 <input checked="" type="checkbox"/>	3.27 <input checked="" type="checkbox"/>	0.14 <input checked="" type="checkbox"/>	8.00 <input checked="" type="checkbox"/>
(Ti ₃₀ Hf ₁₉ Zr ₂₅)(NbTa) ₂₆ Present work	1.55 <input checked="" type="checkbox"/>	2.07 <input checked="" type="checkbox"/>	4.87 <input checked="" type="checkbox"/>	0.11 <input checked="" type="checkbox"/>	4.26 <input checked="" type="checkbox"/>
Fe ₄₄ Ni _{27.5} Co _{16.5} Al ₁₀ Ta ₂ [12]	1.32 <input checked="" type="checkbox"/>	-8.5 <input checked="" type="checkbox"/>	4.81 <input checked="" type="checkbox"/>	0.09 <input checked="" type="checkbox"/>	8.15 <input checked="" type="checkbox"/>
Ti ₅₀ Zr ₂₀ Hf ₁₉ Al ₁₀ Nb ₅ [11]	1.36 <input checked="" type="checkbox"/>	-12.33 <input checked="" type="checkbox"/>	5.87 <input checked="" type="checkbox"/>	0.13 <input checked="" type="checkbox"/>	4.11 <input checked="" type="checkbox"/>
(Ni ₂₇ Cu ₂₃)(Ti ₁₆ Hf ₁₉ Zr ₁₅) [10]	1.58 <input checked="" type="checkbox"/>	-29.08 <input checked="" type="checkbox"/>	10.71 <input checked="" type="checkbox"/>	0.27 <input checked="" type="checkbox"/>	7.23 <input checked="" type="checkbox"/>
(NiCu) ₅₀ (TiHfZr) ₅₀ [6,7]	1.59 <input checked="" type="checkbox"/>	-28.17 <input checked="" type="checkbox"/>	10.66 <input checked="" type="checkbox"/>	0.27 <input checked="" type="checkbox"/>	7.25 <input checked="" type="checkbox"/>
(NiCoCu) ₅₀ (TiHfZr) ₅₀ [8,9]	1.76 <input checked="" type="checkbox"/>	-31.88 <input checked="" type="checkbox"/>	10.85 <input checked="" type="checkbox"/>	0.33 <input checked="" type="checkbox"/>	7.05 <input checked="" type="checkbox"/>
(NiPd) ₅₀ (TiHfZr) ₅₀ [13]	1.59 <input checked="" type="checkbox"/>	-60.35 <input checked="" type="checkbox"/>	9.40 <input checked="" type="checkbox"/>	0.36 <input checked="" type="checkbox"/>	7.00 <input checked="" type="checkbox"/>
Ni ₂₅ Cu ₂₅ Ti ₂₅ Hf ₁₅ Zr ₁₀ [14]	1.55 <input checked="" type="checkbox"/>	-26.05 <input checked="" type="checkbox"/>	10.01 <input checked="" type="checkbox"/>	0.25 <input checked="" type="checkbox"/>	7.25 <input checked="" type="checkbox"/>
BETA III [21;23]	0.9 <input checked="" type="checkbox"/>	-29.08 <input checked="" type="checkbox"/>	10.71 <input checked="" type="checkbox"/>	0.27 <input checked="" type="checkbox"/>	7.23 <input checked="" type="checkbox"/>

☒ Criterion not validated
☐ Criterion validated

Experimental Methods and Characterization

Alloys Preparation and Processing

Ti-26Nb- and Ti-26Nb-like alloys have been prepared and produced by cold crucible from pure metals and master alloys (99.99% Ti, 99.99% Zr, 99.99% Nb, 99.99% Ta and 99.7% Hf97Zr3). All castings have been made under a controlled atmosphere with ultrapure argon. The Ti-26Nb ingot was prepared following the procedure described in Elmay et al. [18]. In the case of the Ti-26Nb-like alloy, to

allow the total dissolution of the 13%at Nb and 13%at Ta in the high-entropy alloy, a ternary alloy Ta₄₀Nb₄₀Zr₂₀ was first produced to serve as a master alloy. It has been then remelted ten times for 20 min to ensure the total melting of Ta in Nb. At the end of this step, the master alloy composition analysis has been verified by energy-dispersive X-ray (EDX) and wavelength-dispersive X-ray spectroscopy (WDS). Then, Ti, Zr, and HfZr have been added during cold crucible melting to obtain the final Ti₃₀Hf₁₉Zr₂₅(NbTa)₂₆ alloy. The ingots of Ti-26Nb alloy and Ti-26Nb-like alloy are afterward homogenized in a homemade

furnace under an ultrapure argon atmosphere. This heat treatment has been performed at 1200 °C for 75 h. The wires of Ti-26Nb alloy and Ti-26Nb-like alloy are solutionized in β phase by a heat treatment at 900 °C for 10 min and followed by a water quench (ST state).

Cold Workability and Heat Treatments

To perform mechanical tests on the same sample geometry, all the commercial and home-prepared alloys have been cold-rolled at room temperature, using groove rollers (Fig. 2b). The rolled samples have, thus, a final square cross-section of $1.5 \times 1.5 \text{ mm}^2$ (Fig. 2a). The BETA III alloy (initial circular cross-section of 6 mm diameter), Ti-26Nb, and Ti-26Nb-like alloys (initial square cross-section of 20 mm side) exhibited good cold workability and their respective cross-sections have been downsized to a square cross-section of $1.5 \times 1.5 \text{ mm}^2$ as described in [40]. The length of Ti-26Nb-like alloy has been increased hence from 80 mm to 14 m with different cold-rolling steps without any intermediate annealing heat treatments. Consequently, the prepared alloy presents very good workability and of the same magnitude as that observed by Lohmuller et al. [40] on a CrMnFeCoNi alloy. The NiTi alloy has an initial circular cross-section of 4 mm diameter; heat treatments have been mandatory after each deformation step of 30% to soften the matrix. Four annealings at 600 °C and deformation steps have been performed to reach a square cross-section of $1.5 \times 1.5 \text{ mm}^2$. The cold-rolling steps and the different heat treatments are summarized in Fig. 2a. Two different metallurgical states have been considered: the cold-worked state (CW) and the annealed one (solution treated or ST). To compare all the alloys at the same

deformation state or heat-treated state, the alloys have been submitted to a solution treatment (ST) just before the last cold-rolling step. During this last step, the deformation rate has been set to 50% for all the alloys and this defines the CW state. It is worth noticing that this value was not reached for the NiTi alloy, a maximum strain of 30% has been then applied instead for this alloy. All heat treatments have been followed afterwards by a water quench (WQ).

Phase Transformation Characterization and Mechanical Testing

First transformation points and free enthalpies of transformation have been measured using a DSC 131 SETARAM. The tests have been conducted following the recommendations of the ASTM standard for the characterization of shape memory alloys [41, 42] with a heating/cooling rate of $10 \text{ }^\circ\text{C min}^{-1}$. Phase analysis has been performed by XRD experiments on a Rigaku diffractometer using Cu-K α radiation (40 kV, 40 mA) at room temperature. The material microstructures have been investigated by scanning electron microscopy (SEM) using a Zeiss Supra 40 SEM, in backscattered emission mode (BSE). To perform in situ measurements, a specific homemade bending sample holder has been set up on the diffractometer and in the SEM chamber.

The superelastic behavior of SMAs is often determined by three-point bending tests according to the ASTM F 2082 [43]. A three-point bending device was previously developed to be used on a large temperature range, from -40 to $200 \text{ }^\circ\text{C}$. These tests have been carried out according to ASTM D790 [44] on a tension/compression universal machine Zwick (Z50) equipped with a thermal chamber.

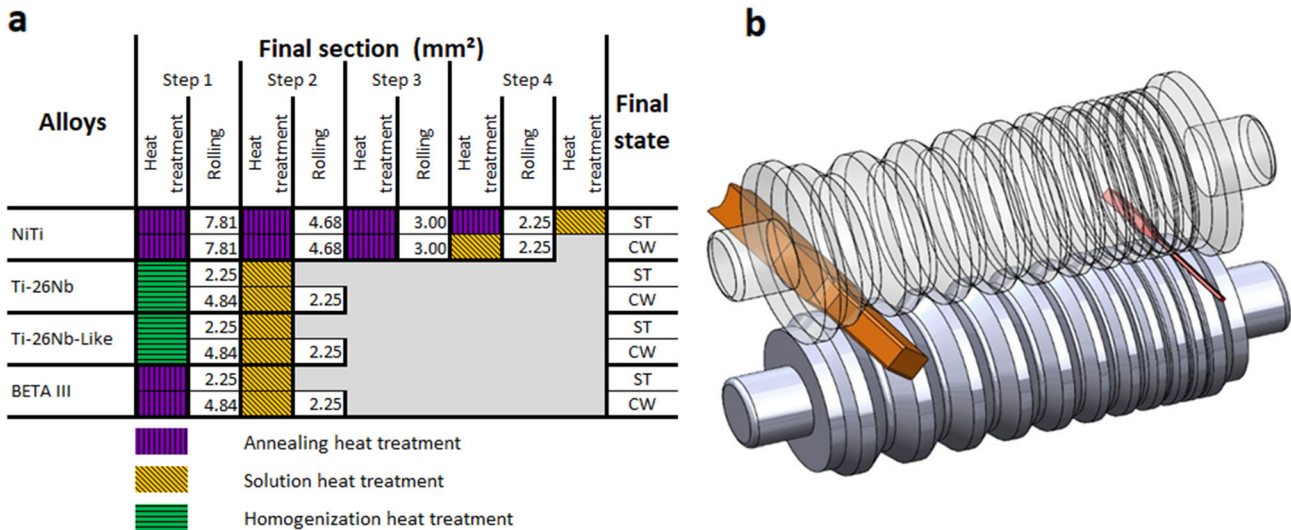


Fig. 2 **a** Heat treatments and rolling steps applied to the four studied alloys. **b** Schematic design of the groove rollers showing schematically the initial and the final rolled wire cross-sections

The ratio between the span length spacing supporting pins (48 mm) and the wire's thickness (1.5 mm) is equal to 32 according to the same testing standard (ASTM D790). The diameter of the central loading support is 50 mm and it limits accordingly the local deformation of a square cross-section wire from $1.5 \times 1.5 \text{ mm}^2$ to a maximum bending deformation of 3%. The bending tests have been achieved at a displacement rate (crosshead speed) of 2 mm min^{-1} . Due to low- (-40°C) and high-temperature (200°C) conditions, it was not possible to use a contact extensometer even if the apparatus is electronically compensated. As the deformation of the machine due to its compliance is compensated, the deflection has been calculated from the crosshead displacement recorded in real-time using the control software (TestXpert).

Experimental Results

Phase Transformation Characterization

Table 2 presents the transformation points of the four alloys after homogenization and ST process. These characteristic temperatures have been deduced from the DSC curves. Fig. 3 shows the DSC curves of Ti-26Nb alloy and Ti-26Nb-like alloy with endothermic and exothermic peaks during the full heating–cooling cycle. On BETA III alloy, it is worth noticing that no peaks were observed as expected [45]. For the first time, it was possible to determine transformation points on the Ti-26Nb alloy by DSC, whereas so far, this determination was only performed through the indirect method as described in [18]. By comparing the Ti-26Nb and Ti-26Nb-like alloys, Fig. 3 shows that the quinary alloy exhibits also direct and reverse phase transformation between austenite and martensite despite the lattice distortion due to high entropy. The transformation points, A_s and A_f , are in the same range for the two alloys. Indeed for the Ti-26Nb alloy, A_s is -17°C and A_f is 50°C , which are very close to those characterizing the transformation in the developed alloy (Ti-26Nb-like), respectively, -20°C and 46°C . However, a slight

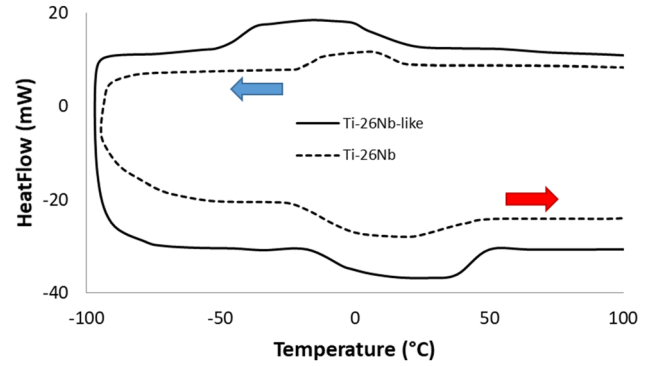


Fig. 3 DSC curve of Ti-26Nb and Ti-26Nb-like alloys in a metallurgical state optimized for DSC samples: heat flow vs. temperature

difference is noticed on the martensitic transformation points: M_s and M_f differ by 11°C and 21°C , respectively. This effect is probably due to the higher distortion of the structures in the HEA version.

To characterize the superelasticity and observe the martensite in the Ti-26Nb-like alloy, the bending micro-device designed for the diffractometer and the SEM chamber is utilized for a maximum applied strain of 2%. When testing curved wires, the samples are held under flexural stress using a homemade bending micro-device before the samples are introduced into the test chamber. At the initial state (Fig. 4a), the microstructure exhibited a single-phase polycrystal as no martensite is visible. XRD pattern (Fig. 4b) confirms the presence of a single body-centered-cubic phase, which is associated with the β phase of TiNb alloys considering the diffraction peak position [18]. This claim means that heat treatment has allowed avoiding omega phase precipitation and martensitic transformation. In the bent configuration, a second phase is observed with SEM both in the tension zone and the compressive zone (Fig. 4c). XRD pattern indicates that a new α'' phase appears and it is counterbalanced by a decrease of β phase peak intensity (Fig. 4d). This indexing is in good agreement with the results obtained by Hussein et al. [46] on a martensitic ternary $\text{Ti}_{77}\text{Nb}_{17}\text{Ta}_6$ alloy and a superelastic TiNbTaO alloy.

Three-Point Bending Static Tests

First, the properties of the alloys are compared in terms of thermomechanical responses when applying two loading–unloading cycles during static three-point bending tests at different temperatures. In the first cycle, loading is performed up to a maximal deflection corresponding to a flexural strain of 3%, followed by unloading (elastic release) down to a 2 N force. Then the second loading cycle is performed up to the same maximal deflection.

Table 2 Transformation temperatures of studied alloys in a metallurgical state optimized for DSC samples

Alloys	Transformation points ($^\circ\text{C}$)			
	A_s	A_f	M_s	M_f
BETA III	–	–	–	–
NiTi	– 37	0	– 40	– 72
Ti-26Nb	– 17	50	17	– 30
Ti-26Nb-like	– 20	46	6	– 51

Fig. 4 SEM observations and diffraction patterns of the ST Ti-26Nb-like alloy: initial state (a, b) and during bending (c, d)

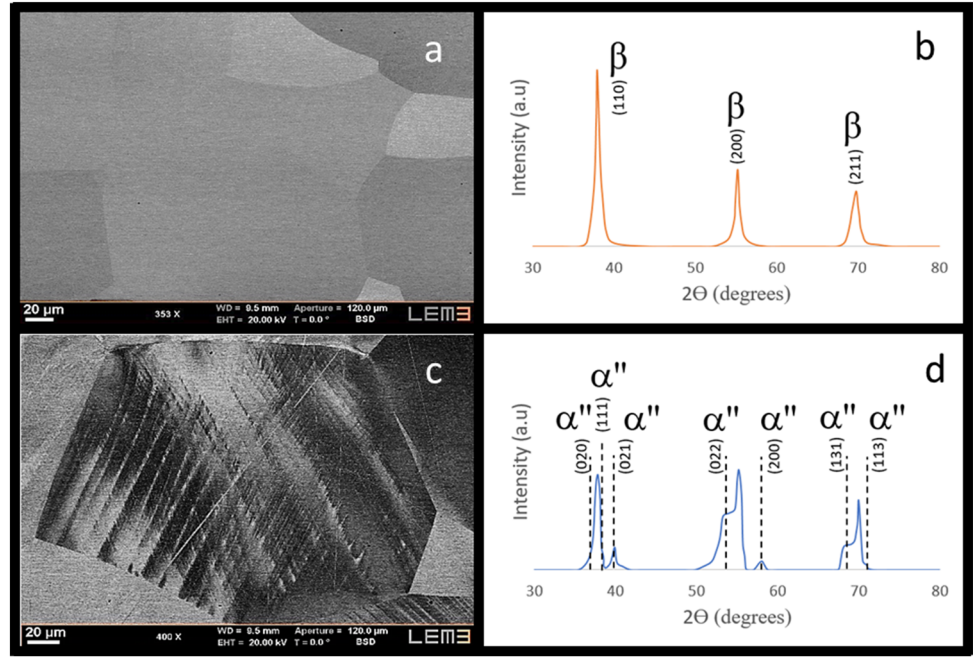


Fig. 5 Three-point bending test curves of the studied alloys between -40 and 200 °C, for two metallurgical states: cold worked (CW) in dashed lines and solution treated (ST) in solid lines. The stresses are estimated in the tension zone of the bent specimen

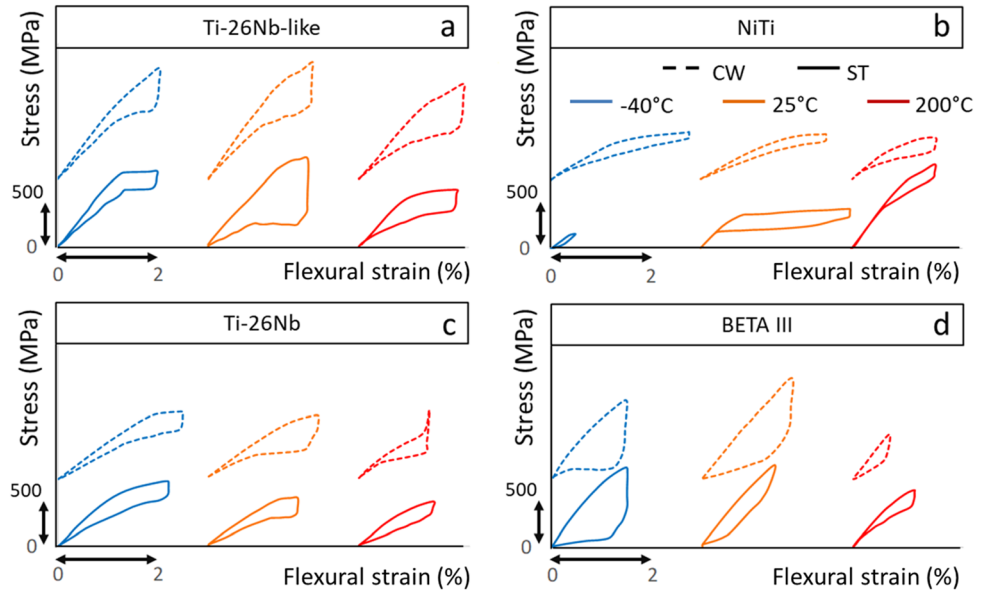


Figure 5 shows the second cycle only, for each alloy at three temperatures; for the sake of readability, the three temperature tests are shifted along the x -axis. In the same way, for each temperature, curves of the CW and ST states have been shifted along the y -axis to make clearer the representation of the experimental stress-strain curves. It is worth mentioning that the bending stresses are estimated in the tension zone of the bent specimen. Whatever the conditions, all the alloys have a residual strain after the first cycle except the NiTi alloy at room temperature. For this reason, the maximal deflection in the second cycle does not correspond to 3% strain as in the first cycle.

For the Ti-26Nb-like alloy (Fig. 5a), a superelastic behavior is observed at room temperature; the reversible strain is about 2%. By comparing ST and CW states, a hardening effect is noticed. Indeed, the maximum stress is increased by a factor around two. At -40 °C and 200 °C, the superelastic behavior is still evidenced for both metallurgical states, with higher stresses at the CW state than for the ST condition. Therefore, this alloy exhibits very stable properties over the studied temperature range. A slight decrease of the elastic modulus is observed with increasing temperature; this effect has been previously observed by Laplanche et al. [47].

Compared to the Ti-26Nb alloy (Fig. 5c), the elastic modulus has increased, as well as the transformation stress and the maximal stress during the thermomechanical cycling. This gives rise to a higher hysteresis too. Figure 5b presents the behavior of the NiTi alloy. It demonstrates the expected superelastic behavior at room temperature for the ST state. Nevertheless, the transformation stress remains much lower than that observed for the Ti-26Nb-like alloy. At low and high temperatures, the behavior of the studied alloy exhibits a degradation. In fact, at $-40\text{ }^{\circ}\text{C}$, the second cycle consists of a very low strain as a residual strain near 3% has been reached after the first cycle; at this temperature, the alloy is almost fully martensitic. At high temperature, an important hardening is observed, compared to the response obtained at room temperature. This hardening is associated with a lower reversible strain since the developed stress becomes superior to that of the Ti-26Nb-like alloy. This effect is discussed more in detail in “Discussion” section.

Finally, the behavior of the BETA III alloy has been considered for comparison (Fig. 5d) as it is known for its athermal behavior. A quite stable pseudoelastic behavior is observed at room temperature and $-40\text{ }^{\circ}\text{C}$, for both ST and CW states. However, at high temperature, the pseudoelastic behavior is reduced: the associated stress level has decreased as well as the hysteresis, opposite to what was observed in our HEA.

Therefore, it can be concluded that the Ti-26Nb-like alloy demonstrates a superelastic behavior and higher stability over the studied range of temperature, whatever the metallurgical states. Moreover, the transformation and maximum stresses are also the highest ones over the four investigated alloys. It can be assumed that lattice distortion brings about an increased stress level. Moreover, conversely to NiTi alloys, the sluggish diffusion associated with HEA is limiting the possible nucleation of the precipitates, leading, hence, to the good thermal stability of the behavior exhibited by the Ti-26Nb-like alloy.

Three-Point Bending Fatigue Tests at $200\text{ }^{\circ}\text{C}$

Besides the comparison based on static bending responses, the experimental analysis of the Ti-26Nb-like alloy and the NiTi alloy is enriched by comparing their isothermal quasi-static fatigue responses during cycling tests at $200\text{ }^{\circ}\text{C}$. Before loading, the samples have been kept at $200\text{ }^{\circ}\text{C}$ for 60 min to reach a uniform temperature distribution in the sample. Then one hundred bending cycles (loading–unloading) have been performed, which corresponds to four hours duration. Between the two loading cycles, the sample was unloaded down to 2 N and kept, thus, for 60 s. Figure 6 presents the loading stress–strain curves for different cycles number (1, 10, 50, 100), for both alloys considered

in the ST (a, c) and CW (b, d) states. For the Ti-26Nb-like ST alloy (Fig. 6a), a slight decrease of the transformation stress is observed for a higher cycle number. For the CW state (Fig. 6b), a higher stress level is observed as expected; however, the maximum stress is decreasing faster with cycling, about 40% less stress between the 10th and 100th cycles. As a consequence, the ST state seems to provide higher thermal stability than the CW one. Moreover, the elastic slope is quite constant for the ST sample, while it decreases for the CW configuration. It must be pointed out that Miyazaki et al. [48] observed similar effect on a TiNb binary alloy. Furthermore, in 2011 Miyasaki’s team [49] concluded that the presence of a large amount of ω -phase can modify the martensitic transformation by hindering the growth of martensite plates. It is worth noticing that excessive formation of ω -phase can also lead to embrittlement of the alloy. Thus, the formation of ω -phase during repeated thermal cycling above $100\text{ }^{\circ}\text{C}$ significantly affects the functional and mechanical stability of β -Ti SMAs. More recently, Sun et al. [50] propose a possible explanation of the observed effect. After cold-rolling and annealing treatment, the β -phase grain size grows from several hundred nanometers to dozens of micrometers, which is far smaller than that of the solution-treated alloy. The morphology of martensite evolves from V-shaped self-accommodated structure to parallel structure. The shape memory effect is hence improved from $< 2\%$ in the solution-treated Ti-16Nb alloy to 3% in the cold-rolled and annealed alloy, whereas they are pre-deformed to 4%. Sun et al. [50] concluded that cold-rolling and post-deformation annealing constitute an effective method to improve the SME of TiNb shape memory alloys.

In addition, the previous effect has been also reported in other works for low cycle fatigue of a pseudoelastic NiTi alloy at room temperature [51] as well as at various temperatures [52]. In these two reference works, the authors have observed a marked decrease of Young’s modulus in the first few cycles which is more pronounced when the applied strain increases. As residual martensite is stabilized during cycling, the effective Young’s modulus becomes an average of austenite and martensite moduli. The results obtained for the NiTi alloy are presented in Fig. 6c and d. A progressive reduction (loss) of superelasticity is observed in both CW and ST states. Indeed, the 100th cycle is not clearly visible as the sample had a permanent strain of 3%. The same trend was obtained by Tyc et al. [53] who studied the tensile fatigue behavior of NiTi wires at high temperatures. The present analysis clearly shows the ability of the developed alloy ($\text{Ti}_{30}\text{Hf}_{19}\text{Zr}_{25}\text{NbTa}_{26}$) as a good candidate for shape memory applications at high temperatures and on a large range of temperatures.

Figure 7a and b show the SEM microstructure study of Ti-26Nb-like alloy samples submitted to the 100 bending

Fig. 6 Three-point bending test results at 200 °C at different cycles number, for the Ti-26Nb-like (a, b) and the NiTi (c, d) alloys

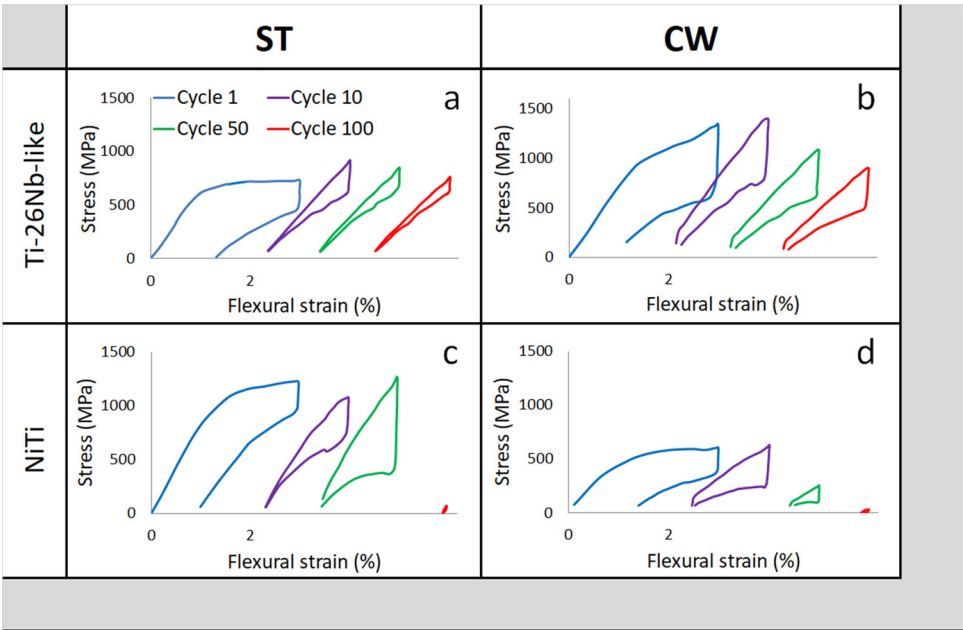
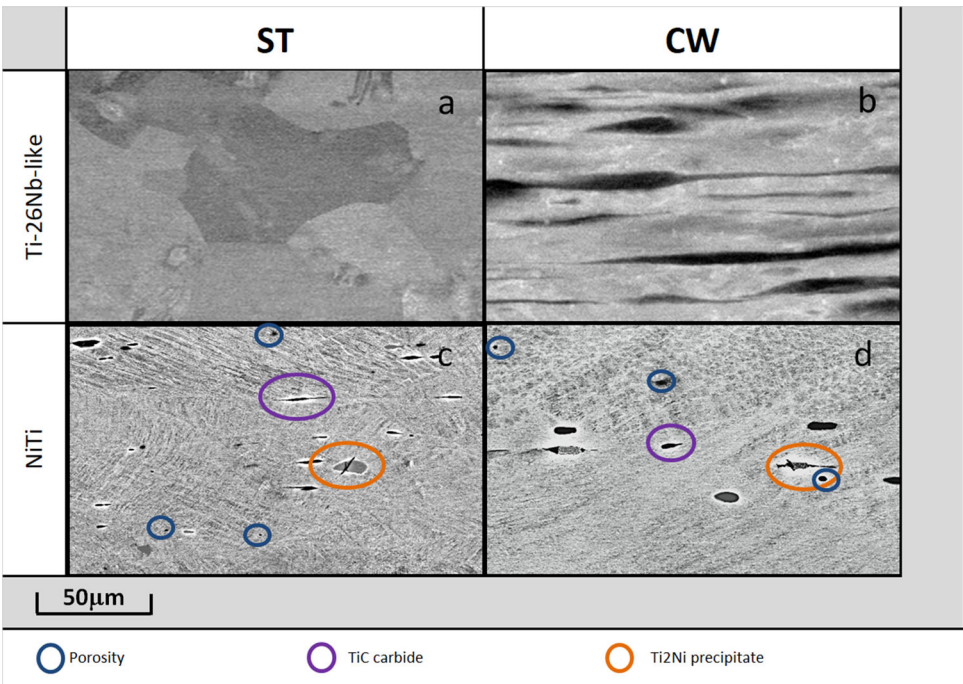


Fig. 7 Microstructure observations after thermal fatigue test for Ti-26Nb-like alloy (a, b) and NiTi alloy (c, d)



cycles at 200 °C. These microstructure observations did not reveal precipitation or crack initiation in the sample. Unlike the Ti-26Nb-like alloy, the NiTi alloy has shown a loss of its elastic behavior (stiffness reduction). Figure 7c and d show the microstructures of the alloy after 100 bending cycles at 200 °C. The presence of martensite, as well as Ti_2Ni precipitates and TiC carbides that promote cracks initiation and propagation can be noticed. These metallic or non-metallic precipitates result from the initial casting of the NiTi ingot [54], but can also be generated by

thermal heat treatments necessary for the transformation of the NiTi ingot [55] into a wire. Cracks present in the Ti_2Ni phase could be induced by the solidification stresses during casting [54], or related to deformation stresses during cold working [56], or also induced by fatigue bending at 200 °C [57]. Ti_2Ni precipitates are at the origin of the rapid aging of the superelastic [58] or pseudoelastic [59] properties of NiTi, especially at high temperatures.

Discussion

The main objective of the present study has been dedicated to answering if the high-entropy effect could provide or lead to a better thermal and mechanical stability of superelastic behavior compared to conventional commercial alloys. A special focus has been devoted to the influence of thermal cycling on these properties for a large range of temperatures (from -40 to 200 °C). Zhang et al. [12] and Wang et al. [11] have shown a superelasticity of 3%, but only at room temperature on their alloys, respectively, FeNiCoAlTaB and Ti-rich TiZrHfAlNb. Li et al. [14] have shown a superelasticity of 2% between 10 and 190 °C in a NiCuTiHf_{0.6}Zr_{0.4}, but the authors did not perform any fatigue test on this alloy. At 200 °C, the Ti-26Nb-like alloy is the only alloy to present an elasticity $> 2\%$ until 100 thermomechanical cycles (Fig. 6), in both metallurgical states (CW, ST). To improve the SMA properties, different ways can be explored such as thermomechanical treatment and/or structural hardening by cold working. The Ti-26Nb-like CW alloy had higher stress than the ST state, but it was less stable during fatigue cycling at 200 °C. Thermomechanical treatments should hence be considered for hardening. Kim et al. [60] have studied TiNb superelastic alloys over a wide composition spectrum Ti-(15–30) at.% Nb, with different thermomechanical treatments. They have obtained a large strain superelasticity recovery (a recovered strain of 4.2%) in TiNb samples with aging heat treatments by increasing the volume fraction of precipitates. Mechanical resistance at high temperatures seems to be correlated to the high-entropy effect. Stepanov et al. have shown that aging a TiHfZrNbTa alloy at 600 °C for 10 h [61] induces a hardness increase of 35% compared to the homogenized state ST (1200 °C, 24 h). This increase is explained by the precipitation of Hf and Ta in the matrix. In this work, no precipitation has been evidenced, as reported in Fig. 7a and b. Sluggish diffusion and cocktail effect may probably preserve HE-SEAs from precipitation and their consequences until 200 °C.

In this paper, the heat treatment conditions applied for small DSC samples and for wire bending specimens are distinct. Indeed, optimized conditions adapted to small samples allowed to reveal the transformation points (temperatures) in a DSC study of Ti-26Nb and Ti-26Nb-like alloys (Fig. 3). However, these specific heat treatments cannot be applied to wired specimens of 100 mm length. The important differences between these two heat treatment modes are the cooling speeds during quenching and the increased gas protection for DSC samples. These differences explain the dissimilarity between the alloy transformation temperatures reported in Table 2 and the

pseudoelastic behavior of Ti-26Nb and Ti-26Nb-like alloys evidenced at -40 °C during the bending tests summarized in Figs. 5 and 6.

To obtain a superelastic effect on a large temperature range, it is worth mentioning that the pseudoelastic alloys are naturally more athermal than SMAs. In addition, due to the pseudoelastic behavior, it is commonly established that the transformation stress in the binary Ti-26Nb alloy is less sensitive to temperature than common SMAs such as NiTi. Indeed, the pseudoelastic behavior is mainly governed by the reorientation of the martensite variants. This justifies hence the fact that the alloys Ti-26Nb and Ti-26Nb-like do not follow the law of Clausius-Capeyron and explains the limited reversible strain exhibited in the stress/strain responses compared to those of NiTi alloy (Fig. 5). This temperature insensitivity characterizing the pseudoelastic behavior of binary TiNb alloys has been patented for the orthodontic applications [62]. It must be noted that the pseudoelastic effect in the Ti-26Nb-like alloy wires can be activated by cold working. Nevertheless, in the ST state of the Ti-26Nb-like alloy wires also appears to be athermal. This temperature insensitivity can be caused either by the heat treatments or by the effects of high entropy such as the strong lattice distortion as well as the cocktail effect.

Fig. 6c and d show the NiTi alloy cyclic responses at 200 °C, and the decreased stress levels in NiTi alloy at CW state can be explained by several aspects as: (i) the recrystallization effect of the NiTi alloy at 200 °C under stress, (ii) the partial restoring effect of the CW state in NiTi alloy at 200 °C under stress, (iii) the effect induced by the reduction of the Ni content in the matrix of the NiTi alloy and in the meanwhile the increase of the precipitate concentration. It is worth noticing in Fig. 6a and b that the Ti-26Nb-like alloy at ST and CW states is preserved from these effects thanks to its high-entropy features.

Conclusion

In this paper, a particular composition has been studied and deeply investigated for its expected superelastic behavior. Superelastic wires have been deformed in bending static loading-unloading tests between -40 to 200 °C and bending isothermal fatigue tests at 200 °C. The main experimental findings can be summarized through the following concluding remarks:

- The TiHfZrNbTa alloy verifies all of the HEA criteria. The (Ti₃₀Hf₁₉Zr₂₅)(NbTa)₂₆ alloy is purely austenitic at room temperature; neither precipitates nor martensite was observed. Moreover, it has shown good cold workability.

- The alloy exhibits a superelastic behavior over the studied range of temperature, demonstrating better thermal stability between -40 and 200 °C than all other studied alloys. The same trend has been observed either on the ST or the CW states. A high-entropy effect can significantly promote the thermal stability of this alloy by preventing the precipitation mechanism.
- During cycling at 200 °C, both ST and CW states still present a superelastic behavior even if the behavior reveals progressive degradation with cycling: the ST alloy is more stable than the CW one. Once again, the developed alloy demonstrates better properties than the conventional alloy. The NiTi alloy had become fully unusable after 100 cycles at 200 °C, due to crack initiation and precipitation. However, the ST version of Ti-26Nb- like $(\text{Ti}_{30}\text{Hf}_{19}\text{Zr}_{25})(\text{NbTa})_{26}$ is more stable than its CW version at 200 °C. Nonetheless, they both present superelastic behavior.

Thus, the $(\text{Ti}_{30}\text{Hf}_{19}\text{Zr}_{25})(\text{NbTa})_{26}$ alloy could be used for its superelasticity from -40 to 200 °C, although its reversible strain is low and limited to 2% in bending conditions. These properties combined with the excellent cold workability of the alloy, make it a promising candidate for superelastic applications at high temperatures.

Acknowledgements This research was supported by the SMART team of the LEM3 laboratory. The authors want to thank sincerely our colleagues and ENSAM/KIT students Timon Carl, Charlene Garot, and Myriam Bensaid who provided help that strongly assisted this study.

References

1. Kim HY, Satoru H, Il KJ et al (2004) Mechanical properties and shape memory behavior of Ti-Nb alloys. *Mater Trans* 45:2443–2448. <https://doi.org/10.2320/matertrans.45.2443>
2. Miyazaki S, Kim HY, Hosoda H (2006) Development and characterization of Ni-free Ti-base shape memory and superelastic alloys. *Mater Sci Eng A* 438–440:18–24. <https://doi.org/10.1016/j.msea.2006.02.054>
3. Kim HY, Fu J, Tobe H et al (2015) Crystal structure, transformation strain, and superelastic property of Ti-Nb-Zr and Ti-Nb-Ta alloys. *Shape Mem Superelasticity* 1:107–116. <https://doi.org/10.1007/s40830-015-0022-3>
4. Elmay W, Patoor E, Gloriant T et al (2014) Improvement of superelastic performance of Ti-Nb binary alloys for biomedical applications. *J Mater Eng Perform* 23:2471–2476. <https://doi.org/10.1007/s11665-014-0876-0>
5. Kim HY, Miyazaki S (2016) Several issues in the development of Ti-Nb-based shape memory alloys. *Shape Mem Superelasticity* 2:380–390. <https://doi.org/10.1007/s40830-016-0087-7>
6. Firstov GS, Kosorukova TA, Koval YN, Odnosum VV (2015) High entropy shape memory alloys. *Mater Today Proc* 2:S499–S503. <https://doi.org/10.1016/j.matpr.2015.07.335>
7. Firstov GS, Kosorukova TA, Koval YN, Verhovlyuk PA (2015) Directions for high- temperature shape memory alloys improvement: straight way to high-entropy materials? *Shape Mem Superelasticity* 1:400–407. <https://doi.org/10.1007/s40830-015-0039-7>
8. Firstova G, Timoshevski A, Kosorukova T et al (2015) Electronic and crystal structure of the high entropy TiZrHfCoNiCu intermetallics undergoing martensitic transformation. *MATEC Web Conf* 33:0–3. <https://doi.org/10.1051/mateconf/20153306006>
9. Yaacoub J, Abuzaid W, Brenne F, Sehitoglu H (2020) Superelasticity of $(\text{TiZrHf})_{50}\text{Ni}_{25}\text{Co}_{10}\text{Cu}_{15}$ high entropy shape memory alloy. *Scr Mater* 186:43–47. <https://doi.org/10.1016/j.scriptamat.2020.04.017>
10. Peltier L, Lohmuller P, Meraghni F et al (2020) Investigation and composition characterization of a “NiTi-like” alloy combining high temperature shape memory and high entropy. *Shape Mem Superelasticity* 6:273–283. <https://doi.org/10.1007/s40830-020-00290-2>
11. Wang L, Fu C, Wu Y et al (2019) Superelastic effect in Ti-rich high entropy alloys via stress-induced martensitic transformation. *Scr Mater* 162:112–117. <https://doi.org/10.1016/j.scriptamat.2018.10.035>
12. Zhang C, Zhu C, Harrington T et al (2018) Multifunctional non-equiatom high entropy alloys with superelastic, high damping, and excellent cryogenic properties. *Adv Eng Mater* 1800941:1–9. <https://doi.org/10.1002/adem.201800941>
13. Canadinc D, Trehern W, Ma J et al (2019) Ultra-high temperature multi-component shape memory alloys. *Scr Mater* 158:83–87. <https://doi.org/10.1016/j.scriptamat.2018.08.019>
14. Li S, Cong D, Sun X et al (2019) Wide-temperature-range perfect superelasticity and giant elastocaloric effect in a high entropy alloy. *Mater Res Lett*. <https://doi.org/10.1080/21663831.2019.1659436>
15. Dirras G, Lilensten L, Djemia P et al (2016) Elastic and plastic properties of as-cast equimolar TiHfZrTaNb high-entropy alloy. *Mater Sci Eng A* 654:30–38. <https://doi.org/10.1016/j.msea.2015.12.017>
16. Feuerbacher M, Heidelmann M, Thomas C (2015) Plastic deformation properties of Zr- Nb-Ti-Ta-Hf high-entropy alloys. *Philos Mag* 95:1221–1232. <https://doi.org/10.1080/14786435.2015.1028506>
17. Elmay W, Patoor E, Bolle B et al (2011) Modification par traitements thermo- mécaniques des propriétés élastiques d’alliages binaires Ti-Nb pour les applications biomédicales. *Congrès français de mécanique (Besancon FRANCE)*
18. Elmay W, Prima F, Gloriant T et al (2013) Effects of thermo-mechanical process on the microstructure and mechanical properties of a fully martensitic titanium-based biomedical alloy. *J Mech Behav Biomed Mater* 18:47–56. <https://doi.org/10.1016/j.jmbbm.2012.10.018>
19. Mussot-Hoinard G, Elmay W, Peltier L, Laheurte P (2017) Fatigue performance evaluation of a Nickel-free titanium-based alloy for biomedical application—effect of thermomechanical treatments. *J Mech Behav Biomed Mater*. <https://doi.org/10.1016/j.jmbbm.2017.02.024>
20. Pelton AR, Dicellol J, Miyazaki S (2000) Optimisation of processing and properties of medical grade Nitinol wire. *Minim Invasive Ther Allied Technol* 9:107–118
21. Laheurte P, Eberhardt A, Philippe MJ (2005) Influence of the microstructure on the pseudoelasticity of a metastable beta titanium alloy. *Mater Sci Eng A* 396:223–230. <https://doi.org/10.1016/j.msea.2005.01.022>
22. Laheurte P, Eberhardt A, Philippe MJ, Deblock L (2007) Improvement of pseudoelasticity and ductility of Beta III titanium alloy—application to orthodontic wires. *Eur J Orthod* 29:8–13. <https://doi.org/10.1093/ejo/cj038>
23. Froes FH, Bomberger HB (1985) Beta titanium alloys. *J Met* 37:28–37

24. Cantor B, Chang ITH, Knight P, Vincent AJB (2004) Microstructural development in equiatomic multicomponent alloys. *Mater Sci Eng A* 375–377:213–218. <https://doi.org/10.1016/j.msea.2003.10.257>
25. Zhou Y, Zhou D, Jin X et al (2018) Design of non-equiatomic medium-entropy alloys. *Sci Rep* 8:1–9. <https://doi.org/10.1038/s41598-018-19449-0>
26. Rehman SU, Khan M, Khan AN et al (2015) Improvement in the mechanical properties of high temperature shape memory alloy (Ti50Ni25Pd25) by copper addition. *Adv Mater Sci Eng*. <https://doi.org/10.1155/2015/434923>
27. König D, Zarnetta R, Savan A et al (2011) Phase transformation, structural and functional fatigue properties of Ti–Ni–Hf shape memory thin films. *Acta Mater* 59:3267–3275. <https://doi.org/10.1016/j.actamat.2011.01.066>
28. Gerstein G, Firstov GS, Kosorukova TA et al (2018) Development of B2 shape memory intermetallics beyond NiAl, CoNiAl and CoNiGa. *Shape Mem Superelasticity* 4:360–368. <https://doi.org/10.1007/s40830-018-0180-1>
29. Dubinskiy SM, Prokoshkin SD, Brailovski V et al (2011) Structure formation during thermomechanical processing of Ti–Nb–(Zr, Ta) alloys and the manifestation of the shape-memory effect. *Phys Met Metall* 112:503–516. <https://doi.org/10.1134/S0031918X11050206>
30. Senkov ON, Scott JM, Senkova SV et al (2011) Microstructure and room temperature properties of a high-entropy TaNbHfZrTi alloy. *J Alloys Compd* 509:6043–6048. <https://doi.org/10.1016/j.jallcom.2011.02.171>
31. Chen SY, Tong Y, Tseng KK et al (2019) Phase transformations of HfNbTaTiZr high-entropy alloy at intermediate temperatures. *Scr Mater* 158:50–56. <https://doi.org/10.1016/j.scriptamat.2018.08.032>
32. Yang G, Zhang T (2005) Phase transformation and mechanical properties of the Ti 50Zr30Nb10Ta10 alloy with low modulus and biocompatible. *J Alloys Compd* 392:291–294. <https://doi.org/10.1016/j.jallcom.2004.08.099>
33. Podolskiy AV, Tabachnikova ED, Voloschuk VV et al (2018) Mechanical properties and thermally activated plasticity of the Ti30Zr25Hf15Nb20Ta10 high entropy alloy at temperatures 4.2–350 K. *Mater Sci Eng A* 710:136–141. <https://doi.org/10.1016/j.msea.2017.10.073>
34. Hume-Rothery W (1966) Atomic diameters, atomic volumes and solid solubility relations in alloys. *Acta Metall* 14:17–20. [https://doi.org/10.1016/0001-6160\(66\)90267-7](https://doi.org/10.1016/0001-6160(66)90267-7)
35. Zhang Y, Zhou YJ, Lin JP et al (2008) Solid-solution phase formation rules for multi-component alloys. *Adv Eng Mater* 10:534–538. <https://doi.org/10.1002/adem.200700240>
36. Guo S, Liu CT (2011) Phase stability in high entropy alloys: formation of solid-solution phase or amorphous phase. *Prog Nat Sci Mater Int* 21:433–446. [https://doi.org/10.1016/S1002-0071\(12\)60080-X](https://doi.org/10.1016/S1002-0071(12)60080-X)
37. Zhang Y, Peng WJ (2012) Microstructural control and properties optimization of high-entrop alloys. *Procedia Eng* 27:1169–1178. <https://doi.org/10.1016/j.proeng.2011.12.568>
38. Yang X, Zhang Y (2012) Prediction of high-entropy stabilized solid-solution in multi-component alloys. *Mater Chem Phys* 132:233–238. <https://doi.org/10.1016/j.matchemphys.2011.11.021>
39. Guo S, Ng C, Lu J, Liu CT (2011) Effect of valence electron concentration on stability of fcc or bcc phase in high entropy alloys. *J Appl Phys*. <https://doi.org/10.1063/1.3587228>
40. Lohmuller P, Peltier L, Hazotte A et al (2018) Variations of the elastic properties of the CoCrFeMnNi high entropy alloy deformed by groove cold rolling. *Materials*. <https://doi.org/10.3390/ma11081337>
41. ASTM F 2004 (2008) Standard test method for transformation temperature of nickel- titanium alloys by thermal analysis
42. Sczerzenie F (2004) Consideration of the ASTM Standards for Ni–Ti alloys. International Conference on Shape memory and superelastic technologies, Baden-Baden, Germany, 3–7 October, pp 203–210
43. ASTM F 2082 (2008) Standard test method for determination of transformation temperature of nickel–titanium shape memory alloys by bend and free recovery
44. ASTM D790 Standard test methods for flexural properties of unreinforced and reinforced plastics and electrical insulating materials. ASTM. <https://doi.org/10.1520/D0790-17>
45. Laino G, De Santis R, Gloria A et al (2012) Calorimetric and thermomechanical properties of titanium-based orthodontic wires: DSC–DMA relationship to predict the elastic modulus. *J Biomater Appl* 26:829–844. <https://doi.org/10.1177/0885328210388678>
46. Hussein AH, Gepreel MAH, Gouda MK et al (2016) Biocompatibility of new Ti–Nb–Ta base alloys. *Mater Sci Eng C* 61:574–578. <https://doi.org/10.1016/j.msec.2015.12.071>
47. Laplanche G, Gadaud P, Perrière L et al (2019) Temperature dependence of elastic moduli in a refractory HfNbTaTiZr high-entropy alloy. *J Alloys Compd* 799:538–545. <https://doi.org/10.1016/j.jallcom.2019.05.322>
48. Miyazaki S, Imai T, Igo Y, Otsuka K (1986) Effect of cyclic deformation on the pseudoelasticity characteristics of Ti–Ni alloys. *Metall Trans A Phys Metall Mater Sci* 17 A:115–120. <https://doi.org/10.1007/BF02644447>
49. Al-Zain Y, Kim HY, Koyano T et al (2011) Anomalous temperature dependence of the superelastic behavior of Ti–Nb–Mo alloys. *Acta Mater* 59:1464–1473. <https://doi.org/10.1016/j.actamat.2010.11.008>
50. Sun B, Meng XL, Gao ZY et al (2017) Effect of annealing temperature on shape memory effect of cold-rolled Ti–16 at.%Nb alloy. *J Alloys Compd* 715:16–20. <https://doi.org/10.1016/j.jallcom.2017.04.275>
51. Maletta C, Sgambitterra E, Furguele F et al (2014) Fatigue properties of a pseudoelastic NiTi alloy: strain ratcheting and hysteresis under cyclic tensile loading. *Int J Fatigue* 66:78–85. <https://doi.org/10.1016/j.ijfatigue.2014.03.011>
52. Miyazaki S, Imai T, Igo Y, Otsuka K (1986) Effect of cyclic deformation on the pseudoelasticity characteristics of Ti–Ni alloys. *Metall Mater Trans A*. <https://doi.org/10.1007/BF02644447>
53. Tyc O, Heller L, Vronka M, Šittner P (2020) Effect of temperature on fatigue of superelastic NiTi wires. *Int J Fatigue* 134:105470. <https://doi.org/10.1016/j.ijfatigue.2020.105470>
54. Patel M, Plumley D, Bouthot R, Proft J (2006) The effects of varying active Af temperatures on the fatigue properties of nitinol wire. In: Medical device materials III—Proceedings of the materials and processes for medical devices conference, vol 2005, pp 148–153
55. Tyc O, Pilch J, Šittner P (2016) Fatigue of superelastic NiTi wires with different plateau strain. *Procedia Struct Integr* 2:1489–1496. <https://doi.org/10.1016/j.prostr.2016.06.189>
56. Sadrnezhad SK, Raz SB (2008) Effect of microstructure on rolling behavior of NiTi memory alloy. *Mater Manuf Process* 23:646–650. <https://doi.org/10.1080/10426910802316526>
57. Wagner MFX, Dey SR, Gugel H et al (2010) Effect of low-temperature precipitation on the transformation characteristics of Ni-rich NiTi shape memory alloys during thermal cycling. *Intermetallics* 18:1172–1179. <https://doi.org/10.1016/j.intermet.2010.02.048>
58. Yamashita F, Ide Y, Kato S et al (2019) Effect of nonmetallic inclusions on fatigue properties. *Metals* 9(9):7–11

59. Rahim M, Frenzel J, Frotscher M et al (2013) Impurity levels and fatigue lives of pseudoelastic NiTi shape memory alloys. *Acta Mater* 61:3667–3686. <https://doi.org/10.1016/j.actamat.2013.02.054>
60. Kim HY, Ikehara Y, Kim JI et al (2006) Martensitic transformation, shape memory effect and superelasticity of Ti–Nb binary alloys. *Acta Mater* 54:2419–2429. <https://doi.org/10.1016/j.actamat.2006.01.019>
61. Stepanov ND, Yurchenko NY, Zherebtsov SV et al (2018) Aging behavior of the HfNbTaTiZr high entropy alloy. *Mater Lett* 211:87–90. <https://doi.org/10.1016/j.matlet.2017.09.094>
62. Filleul MP, Laheurte P, Terrasse JM et al (2015) Ressort d'orthodontie hélicoïdal et son procédé de fabrication. Office européen des brevets, Munich, European patent. #EP3009153A1-2016/16

Publisher's Note Springer Nature remains neutral with regard to jurisdictional claims in published maps and institutional affiliations.